ACS APPLIED NANO MATERIALS

www.acsanm.org Article

A Nickel Telluride Electrochemical Sensor for the Detection of the Antibiotic Ronidazole

Tara Barwa, Ramaraj Sukanya, Thamaraiselvi Kanagaraj, Gillian Collins, Yiran Luo, Eithne Dempsey, Raj Karthik, Jae-Jin Shim, and Carmel B. Breslin*

Cite This: *ACS Appl. Nano Mater.* 2025, 8, 20523−20533 Read Online

ACCESS | Metrics & More | Article Recommendations | Supporting Information

ABSTRACT: The widespread use of nitroimidazole antibiotics such as ronidazole (RON) in human and veterinary medicine raises concerns about environmental persistence and antimicrobial resistance. Sensitive detection of trace RON in water is therefore essential. Here, we report for the first time, nickel telluride nanoparticles (NiTe NPs) as an electrochemical sensor specifically designed for RON detection. NiTe, a transition metal chalcogenide with high conductivity and electrocatalytic activity, was synthesized via a simple hydrothermal method and characterized by X-ray diffraction, field-emission scanning electron microscopy, transmission electron microscopy, and X-ray photoelectron spectroscopy. When drop-cast on a glassy carbon electrode, the NiTe NPs significantly enhanced electron transfer and promoted efficient electrochemical reduction of RON. The sensor achieved a detection limit of 1.5 nM, a wide linear range of 0.01−270 μM, and a sensitivity of 0.489 μA μM^{-1} cm^{-2}. It also displayed excellent selectivity against common interferents and maintained stability and reproducibility during extended testing. Application to spiked tap and river water confirmed accurate recovery. This work highlights NiTe as an underutilized telluride-based material and establishes its novel application in the environmental monitoring of antibiotic contaminants, addressing a critical gap in electrochemical sensing research.

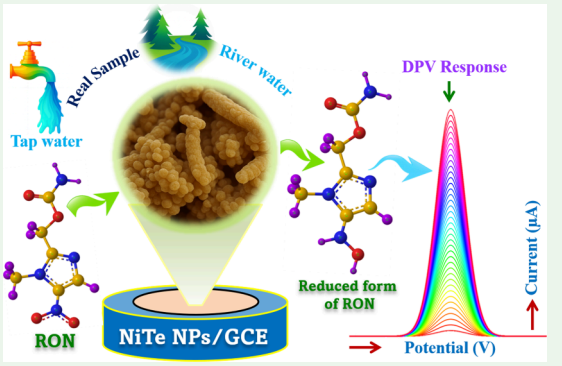

KEYWORDS: *electrochemical sensor, nickel telluride nanoparticles, ronidazole, environmental monitoring, antimicrobial resistance*

INTRODUCTION

Antibiotics have redefined medicine by effectively treating bacterial infections and reducing morbidity and mortality worldwide. However, their extensive and often indiscriminate use has led to the emergence of antimicrobial resistance (AMR), posing a serious threat to global public health.[1,2] The World Health Organisation (WHO) recognizes AMR as one of the top ten global public health threats facing humanity.[2,3] A key contributor to AMR is the contamination of environmental matrices with residual antibiotics from pharmaceutical manufacturing, hospital waste, livestock farming, and human excretion.[4] These residual antibiotics persist in water and soil systems, exerting selective pressure that supports resistance even at very low concentrations. Given the environmental and clinical implications, it is becoming crucial to monitor antibiotics at trace levels in complex matrices.[4]

Among various analytical methods, electrochemical sensors have attracted significant attention due to their low cost, portability, rapid response, high sensitivity, and ease of fabrication. While alternative approaches such as liquid chromatography−mass spectrometry (LC−MS), fluorescence photometry, capillary electrophoresis, and fluorescent labeling have been employed for drug detection, these techniques, although highly sensitive and selective, often suffer from certain drawbacks. They generally require costly instrumentation, labor-intensive sample pretreatment, and skilled personnel to operate, in addition to being time-consuming with relatively long detection periods.[5−7] In contrast, electrochemical sensing provides a simpler, faster, and more cost-effective strategy, which motivated its selection in the present study for RON detection.[8,9] The performance of electrochemical sensors strongly depends on the properties of the electrode material, making the development of novel, efficient, and stable sensing materials essential.[10] RON is a member of the nitroimidazole family, a well-known class of antibiotics. These drugs are used to treat protozoal infections and anaerobic bacterial diseases in both humans and animals, and can enter aquatic environments through agricultural runoff.[11] Among them, RON, a 5-nitroimidazole derivative, is widely used for treating histomoniasis and trichomoniasis in poultry and hemorrhagic enteritis in pigs, and anaerobic infections.[12] A

Received: August 15, 2025
Revised: October 3, 2025
Accepted: October 6, 2025
Published: October 13, 2025

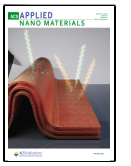

significant portion of the compound is excreted through urine and faeces after administration, which contributes to its release into the environment, making it a hazardous environmental pollutant.[12−14] Nevertheless, its structure, containing a nitro group, enables redox activity under electrochemical conditions, providing an avenue for sensitive detection. For example, Priya et. al[13] discussed a zinc−chromium layered double hydroxide with nickel−cobalt sulfide (ZC/NCS) to detect RON, resulting in a sensitivity of 0.374 μA μM^{-1} cm^{-2} and a low detection limit of 1.1 nM.[13] Furthermore, Vemulguran et al. described a praseodymium tungsten oxide, with a high sensitivity of 7.72 μA μM^{-1} cm^{-2}, for the detection of RON.[14] Modifying the sensor surface with electroactive materials significantly improves sensor sensitivity and selectivity by facilitating better analyte interaction.[15]

Recent advances have highlighted the potential of transition metal chalcogenides (TMCs), particularly metal tellurides, for a wide range of electrochemical applications due to their distinctive physical and chemical properties.[16] Among the chalcogen elements, tellurium (Te) has greater electrical conductivity compared to sulfur and selenium.[17] These characteristics enable telluride-based materials to support efficient electron transfer, a key factor for applications such as electrochemical sensing.[16,18,19] With their high intrinsic conductivity, tunable electronic band structures, and good surface chemistry, metal tellurides are emerging as promising materials for high-performance electrochemical systems.[19] In addition to cobalt-based tellurides, other compositions such as nickel tellurides (e.g., NiTe, Ni_3Te_2) and nickel−cobalt tellurides have shown considerable potential in electrochemical applications. For instance, Wang et al.[20] employed hydrothermal synthesis to produce $CoNiTe_2$ nanorods and developed a novel $CoNiTe_2$/Nafion/GCE for use as a nonenzymatic electrochemical sensor for dopamine.[20] The NiTe-based systems exhibit excellent electron transport properties and a high density of electroactive sites, which can be beneficial in sensing applications.[21] Their chemical and mechanical properties further support their integration into the electrode structure for sensitive and stable performance. Moreover, the Te−metal bond properties in these materials allow for the modulation of electronic structure and surface reactivity, which can be tailored to enhance analyte-specific interactions, critical for achieving high selectivity in electrochemical sensing platforms.[21] In another study, Mayilmurugan et al.[21] reported the use of NiCoTe nanorods (NRs) as an electrode material for nonenzymatic hydrogen peroxide (H_2O_2) detection, demonstrating its dual functionality as a biosensor for endogenous H_2O_2 and an optical limiter. Similarly, Golrokh Amin et al.[22] described the development of an ultrasensitive and highly selective nonenzymatic glucose sensor based on Ni_3Te_2 nanostructures, where they demonstrated that Ni_3Te_2 exhibited excellent electrocatalytic activity toward glucose oxidation at an extremely low working potential, offering high sensitivity, selectivity, and stability.[22] While recent studies have demonstrated the potential of telluride-based materials in electrochemical sensing, their use remains comparatively limited relative to the more extensively studied sulfide- and selenide-based systems.[16] In particular, applications of nickel telluride for the detection of antibiotic pollutants are largely unexplored, providing a unique opportunity to expand their scope. The favorable electrocatalytic surface properties of metal tellurides can be exploited to enhance redox reactions involving diverse analytes, including antibiotics. Indeed, recent reports on NiTe nanorods and CoTe nanosheets for biosensing and chemical detection have shown promising sensitivity, stability, and reproducibility.[22−24] However, further research is required to optimize their morphology, composition, and interfacial properties in order to fully harness their potential for detecting emerging contaminants such as antibiotic drugs. In the present work, we address this gap by synthesizing nickel telluride nanoparticles (NiTe NPs) with controlled morphology and uniform distribution via a simple hydrothermal method, yielding well-defined crystalline structures with high electroactive surface area. By integrating these optimized NiTe NPs onto a glassy carbon electrode, we establish a robust interface that enhances electron transfer, thereby enabling the sensitive and selective electrochemical detection of RON.

Therefore, this study explores the NiTe NPs as a single-component electrode modifier for detecting RON. By utilizing the redox activity of RON and the electrochemical properties of NiTe NPs, it provides a sensitive and selective platform. By addressing antibiotic residues in environmental water, this work contributes to the field of environmental sensing.

EXPERIMENTAL SECTION

Materials. The chemicals employed consisted of nickel(II) nitrate hexahydrate $Ni(NO_3)_2.6H_2O$, potassium tellurate (K_2TeO_4), hydrazine monohydrate ($N_2H_4.H_2O$), 98%) and pure ethanol (98%). Other chemicals included potassium hydroxide (KOH), hydrochloric acid (HCl), zinc chloride ($ZnCl_2$), magnesium chloride ($MgCl_2$), calcium chloride ($CaCl_2$), copper(II) chloride ($CuCl_2$), ammonium chloride (NH_4Cl), sodium nitrate ($NaNO_3$), sodium carbonate (Na_2CO_3), sodium chloride (NaCl), and sodium sulfate (Na_2SO_4). Antibiotic drugs involved RON, sulfanilamide (SFL), levofloxacin (LVF), ciprofloxacin (CPL), enrofloxacin (ENR) and the analgesic drug paracetamol. All chemicals were of AnalaR grade reagents and were purchased from Sigma-Aldrich. Deionized water was used in the preparation of the solutions, which were deoxygenated with high-purity nitrogen gas. All experiments were performed in triplicate at room temperature.

Instrumentation. The structural properties of the composite were analyzed using X-ray diffraction (XRD) with an XPERT-PRO diffractometer (PANalytical B.V., The Netherlands) equipped with Cu K_α radiation (λ = 1.5406 Å). Surface chemical composition and elemental states were analyzed by X-ray photoelectron spectroscopy (XPS) on a Thermo Scientific Instruments (USA) Al−K_α X-ray source system. Morphological and elemental analyses were conducted using field emission scanning electron microscopy (FE-SEM; Hitachi S-4800) coupled with energy-dispersive X-ray spectroscopy (EDS). Transmission electron microscopy (TEM) was carried out on a FEI Titan Themis Cubed G2 60−300 kV double-aberration-corrected monochromated instrument coupled with FEI Talos F200i-Acceleration voltage 200 kV, Bruker Xflash, 129 eV for EDX elemental analysis. The average particle size from the TEM images was determined using ImageJ software.

Synthesis of Nickel Telluride Nanoparticles. In a typical synthesis, 20 mL of 0.02 M $Ni(NO_3)_2$ was prepared in deionized water under stirring to form a homogeneous solution. Separately, 1 mL of N_2H_4, 5 mL of ethanol, and K_2TeO_4 were combined and dissolved in 10 mL of deionized water to give a 0.02 M K_2TeO_4 solution. This K_2TeO_4 solution was then slowly added to the $Ni(NO_3)_2$ solution under continuous stirring. The combined mixture was then stirred for an additional hour. The final solution was brought up to a total volume of 50 mL with deionized water and transferred to a Teflon-lined stainless-steel autoclave for hydrothermal treatment at 180 °C for 12 h. After the reaction, the autoclave was allowed to cool naturally to room temperature. The resulting black-colored product was collected, thoroughly washed with deionized water and ethanol,

https://doi.org/10.1021/acsanm.5c03794
ACS Appl. Nano Mater. 2025, 8, 20523−20533

Figure 1. Schematic illustration of the hydrothermal synthesis of nickel telluride nanoparticles (NiTe NPs).

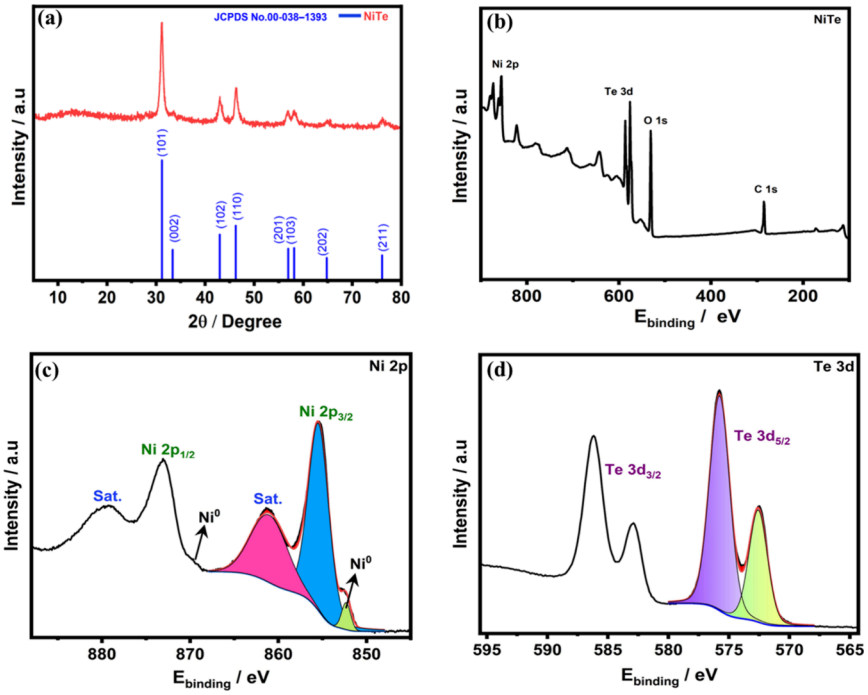

Figure 2. (a) XRD, (b) XPS survey spectrum, (c) Ni 2p and (d) Te 3d high-resolution spectra recorded for NiTe NPs.

and dried at 50 °C overnight. A schematic illustration of the synthesis of the NiTe NPs by the hydrothermal method is shown in Figure 1.

Preparation of the Electrode for Sensing. To prepare the sensing electrode, the NiTe NPs powder was first dispersed in a mixed solvent of ethanol and deionized water in a 1:1 ratio (by volume) at a concentration of 2 mg mL^{-1} (optimized concentration). The mixture was ultrasonicated for 10 min to ensure uniform dispersion and to produce a stable and homogeneous suspension. Prior to modification, the GCE was polished with 1 μm diamond suspensions (Akasol) on a polishing microcloth, rinsed thoroughly with deionized water, and dried. Subsequently, 10 μL of the NiTe suspension (optimized) was drop-cast onto the clean surface of the GCE and allowed to dry under an infrared lamp.

Electrochemical Measurements. Electrochemical measurements were performed in a conventional three-electrode setup, made up of a glassy carbon electrode (GCE, geometric area = 0.0707 cm^2) as the working electrode, a saturated calomel electrode (SCE) as the reference electrode, and a platinum wire as the counter electrode. A 0.05 M KOH solution was prepared and then carefully adjusted to pH 8.0 by the controlled addition of HCl. This adjustment resulted in a solution containing K^+, OH^-, and Cl^- ions, maintaining an ionic strength of approximately 0.05 M while providing a mildly alkaline medium required for RON reduction, and a solution in which the NiTe NPs were highly stable. In the pH study, a similar process was carried out by adjusting the pH to lower pH values using HCl. To estimate the electroactive surface area of the modified electrodes, cyclic voltammetry (CV) was performed using a 3 mM $[Ru(NH)_6]^{3+}$ redox probe dissolved in 0.1 M NaCl.

All electrochemical experiments were performed at ambient temperature. Prior to measurements, all solutions were thoroughly deoxygenated by purging with high-purity nitrogen gas for 30 min to eliminate dissolved oxygen. CV was conducted using a Solartron 1285 potentiostat (USA) at a scan rate of 75 mV s^{-1}, unless stated otherwise. Electrochemical impedance spectroscopy (EIS) was performed in the same drug solution using a Solartron 1255 Frequency Response Analyzer, paired with a Solartron 1287 potentiostat. Impedance spectra were recorded over a frequency range of 100 kHz to 5 mHz with an applied sinusoidal perturbation of 10 mV. To ensure stability and reproducibility, all electrodes were preconditioned for 30 min before data collection in the RON-containing solution. The resulting EIS data were analyzed by fitting to appropriate equivalent circuit models.

Differential pulse voltammetry (DPV) measurements were performed using a CHI440 electrochemical workstation (CH Instruments, USA). The experimental parameters included a pulse amplitude of 50 mV, a pulse width of 0.05 s, a sampling interval of 0.0167 s, and a pulse period of 0.5 s. The resulting data were analyzed

https://doi.org/10.1021/acsanm.5c03794
ACS Appl. Nano Mater. 2025, 8, 20523−20533

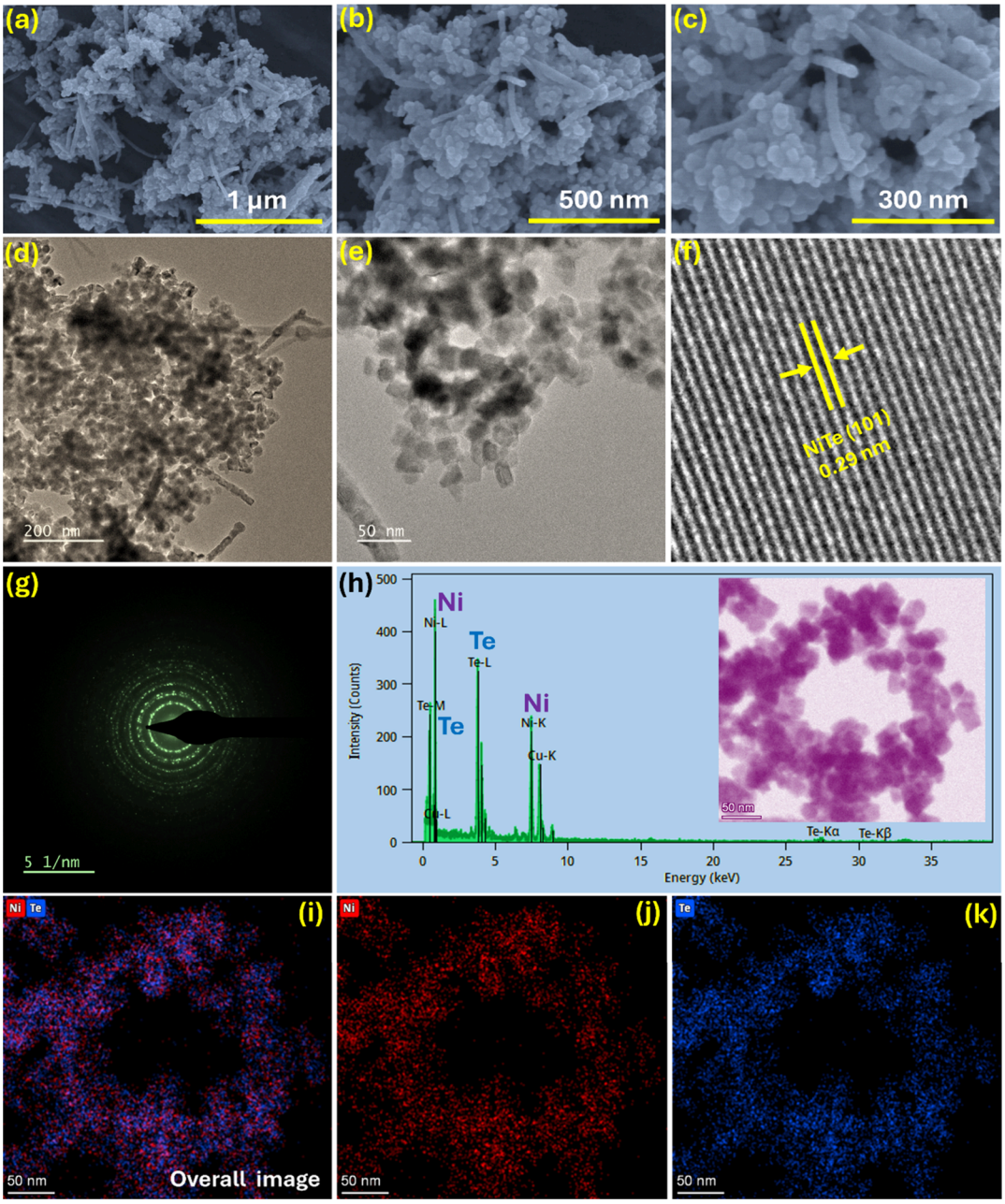

Figure 3. (a–c) FE-SEM images of NiTe NPs at different magnifications, (d, e) TEM and HR-TEM images of NiTe NPs, (f) lattice fringe image, (g) SAED pattern, (h) EDS spectrum with HAADF image shown in the inset, (i–k) elemental mapping images showing the distribution of Ni and Te in NiTe NPs.

for statistical consistency, and both standard errors and relative standard deviations (%RSD) were calculated to assess precision.

Real Water Samples. To evaluate the performance of the sensor in real conditions, two types of water samples were tested: tap water obtained from the laboratory and freshly collected river water from Rye River, Maynooth, Ireland. Before analysis, both samples underwent centrifugation to remove suspended particulates, followed by filtration. RON was spiked into each water sample at different known concentrations, and the resulting current response was measured and analyzed. To determine the accuracy of the sensor in complex matrices, the measured currents were compared to similar known concentrations prepared in deionized water, and the percentage recovery was calculated accordingly.

RESULTS AND DISCUSSION

Characterization of NiTe NPs. As shown in the scheme in Figure 1, the NiTe NPs were synthesized using a one-step hydrothermal synthesis method. In summary, $Ni(NO_3)_2.6H_2O$ and K_2TeO_4 served as the sources of Ni and Te ions, respectively, while $N_2H_4.H_2O$ was used as the reducing agent. Figure 2a shows the XRD pattern of the NiTe NPs, which was used to determine the crystallinity and phase structure. The results in the figure demonstrate the presence of characteristic diffraction peaks of NiTe NPs with a hexagonal crystal structure relating to diffraction angles of 30.8, 42.8, 45.7, 56.1, 58, 64.3 and 75.2° corresponding to (101), (102), (110), (201), (103), (202) and (211) planes, respectively as per JCPDS No. 00-038-1393.[25]

https://doi.org/10.1021/acsanm.5c03794
ACS Appl. Nano Mater. 2025, 8, 20523–20533

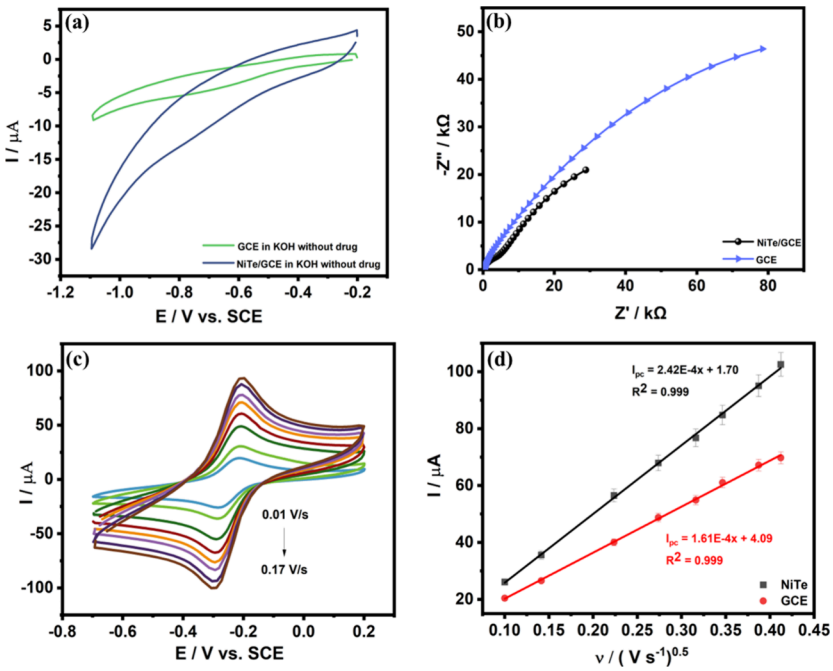

Figure 4. (a) CVs recorded for GCE and NiTe/GCE at pH 8.0, (b) Nyquist plots recorded for GCE and NiTe/GCE at −0.68 V in 300 μM RON at pH 8.0, (c) CVs recorded for NiTe/GCE in 3 mM $Ru(NH_3)_6^{3+}$ in 0.1 M NaCl and (d) corresponding peak current plotted against the square root of the scan rate for NiTe/GCE and GCE.

The crystallite size of NiTe NPs was estimated from the XRD pattern by applying the Scherrer relation (eq 1).

$$D = K\lambda/\beta\cos\theta \quad (1)$$

In this expression, D corresponds to the mean crystallite dimension, K is the shape factor (taken as 0.9), λ is the incident X-ray wavelength (1.514 Å), β is the full width at half-maximum (FWHM) of the selected diffraction peak, and θ is the Bragg diffraction angle. Using this approach, the average crystallite size of the prepared NiTe NPs sample was found to be approximately 10 nm.

Furthermore, the chemical constituents and surface composition of the NiTe NPs were measured by XPS. The XPS survey spectra in Figure 2b display characteristic signals corresponding to nickel (Ni), tellurium (Te), and carbon (C). The carbon peak likely originates from the residual carbon background. In Figure 2c, the XPS spectra of Ni 2p, i.e., Ni^{2+}, Ni^0, and satellite peaks are shown in the spectra. The peaks at 855.4 and 873.1 eV can be attributed to Ni^{2+} $2p_{3/2}$ and Ni^{2+} $2p_{1/2}$, respectively. The peaks at about 860.8 and 879.0 eV are assigned to the corresponding shakeup satellite peaks. In addition, the Ni 2p spectrum exhibits two closely spaced peaks at binding energies of 852.3 and 869.5 eV, which are attributed to metallic nickel (Ni^0). These peaks may arise from the reduction of Ni^{2+} ions facilitated by the hydrazine reducing agent in the reaction.[25] The binding energy of Te 3d in Figure 2d shows prominent peaks at 572.5 and 582.9 eV, corresponding to Te $3d_{5/2}$ and Te $3d_{3/2}$ in NiTe, respectively. The two peaks at 575.7 and 586.1 eV are related to the surface oxidation species of Te. Overall, the XPS spectra confirm the presence of oxidized Ni and Te species in addition to the metallic NiTe signals. These oxide-related peaks originate from surface oxidation of the nanoparticles upon exposure to air, while the bulk phase remains crystalline NiTe, as verified by XRD and HR-TEM. Thus, the material is best described as NiTe nanoparticles with surface oxides.

The structural and morphological features of the NiTe NPs were characterized through FE-SEM and HR-TEM analyses. As illustrated in Figure 3a−c, the FE-SEM images with different magnifications reveal that the NiTe NPs exhibit an elliptical morphology and tend to aggregate and seed, leading to the formation of nanorod-like structures with accessible reactive sites. Correspondingly, TEM and HR-TEM images, shown in Figure 3d,e, display well-defined NiTe NPs with an average size of approximately 17.9 nm. In addition, the analysis reveals lattice fringes, corresponding to interplanar spacings of approximately 0.29 nm, suggesting well-ordered crystalline planes within the NiTe structure. These lattice fringes are attributed to the (101) plane of NiTe (Figure 3f), which is in good agreement with the XRD results, Figure 2a. Selected area electron diffraction (SAED) was employed to complement the TEM analysis and to provide information on the crystallinity of the NiTe NPs. The SAED pattern in Figure 3g displays a series of well-defined concentric diffraction rings, confirming the crystalline nature of the sample. The observed ring spacings correspond well to the (101), (102), (110), (201), and (202) planes identified by XRD, further confirming the crystallinity of NiTe. The continuous ring distribution, rather than discrete diffraction spots, indicates that the nanoparticles are randomly oriented and crystalline in nature. These findings are consistent with the TEM and HR-TEM observations, providing complementary evidence for the structural uniformity of the NiTe NPs. The high-angle-annular dark-field (HAADF) image (inset of Figure 3h) and the elemental mapping shown in Figure 3i−k clearly demonstrate a uniform spatial distribution of Ni and Te across the sample, with no detectable impurities. Additionally, the EDX spectrum in Figure 3h further confirms the presence of the expected elements, validating the successful synthesis and composition of the NiTe NPs.

The TEM image shown in supporting data, Figure S1a, indicates that the NiTe NPs are nearly spherical and tend to form aggregated clusters. To further analyze their size

https://doi.org/10.1021/acsanm.5c03794
ACS Appl. Nano Mater. 2025, 8, 20523−20533

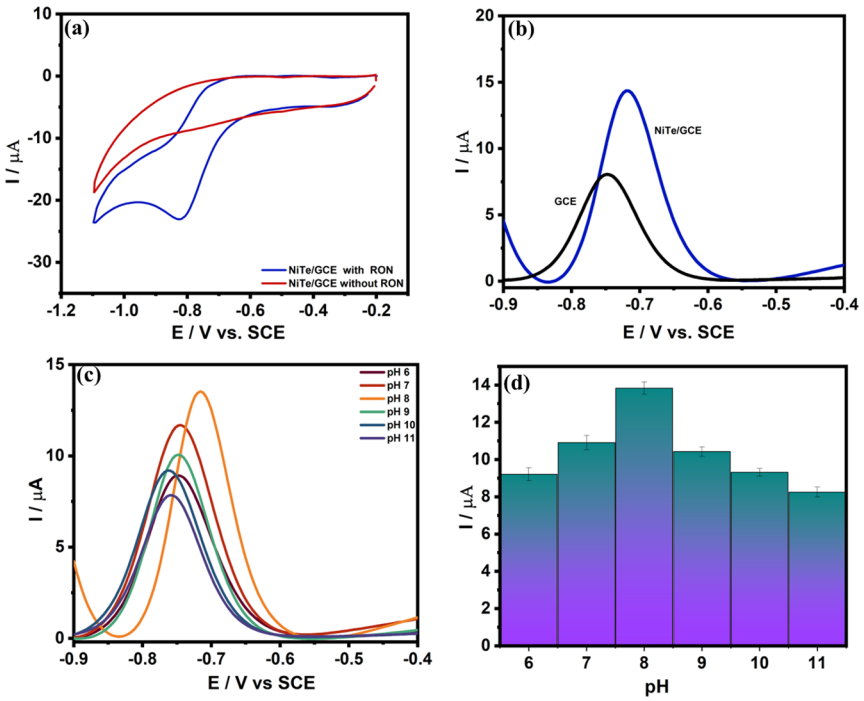

Figure 5. (a) CVs of NiTe/GCE in 300 μM RON and in drug-free supporting KOH electrolyte, (b) DPVs for GCE and NiTe/GCE in 300 μM RON at pH 8.0 (where the reduction of RON is presented as a positive current), (c) DPVs of NiTe/GCE at pH values from 6.0 to 11.0 and (d) peak current plotted as a function of pH in 300 μM RON.

distribution, a particle size histogram was plotted from the TEM measurements (Figure S1b). The histogram reveals that the particle sizes are mainly distributed between 14 and 22 nm, with an average particle size of ~17.9 nm. This value is in close agreement with the crystallite size (~10 nm) estimated from XRD using the Scherrer equation, confirming consistency between XRD and TEM analyses.

Electrochemical Detection of Ronidazole. Initially, the electrochemistry of NiTe/GCE and GCE was compared at a pH of 8.0. The corresponding CVs, shown in Figure 4a, were recorded in the absence of the target analyte, RON. The CV curves reveal a significant difference in response between the two electrode systems. The NiTe/GCE exhibits much higher cathodic and anodic currents compared to the bare GCE, indicating enhanced electrochemical activity upon modification of the electrode surface with NiTe NPs. This enhancement can be attributed to the improved conductivity and increased electroactive surface area of the NiTe/GCE. To further probe these differences in electrochemical activity, impedance data were recorded for the NiTe/GCE and GCE, again at a pH of 8.0, but with the addition of 300 μM RON. The resulting Nyquist plot, presented in Figure 4b, compares the bare GCE and the GCE modified with NiTe NPs. The NiTe/GCE exhibits lower impedance at comparable frequencies, as depicted in the Nyquist plot, where the NiTe/GCE electrode shows a smaller semicircular arc compared to the bare GCE. This indicates a lower charge transfer resistance at the NiTe/GCE interface, which is attributed to the improved electron transfer kinetics offered by NiTe NPs. This is consistent with the data presented in Figure 4a. These data were further analyzed by fitting the data to a two-time constant model, with a solution resistance, a double layer capacitance, C_{dl}, in parallel with the charge-transfer resistance (R_{ct}) and a second couple that includes a constant-phase element (CPE) and a resistor (R_2). The overlap between the data generated by this model and the experimental data is excellent, allowing for a good estimation of circuit parameters. Interestingly, the C_{dl} was estimated at 20.93 ± 0.7 μF for NiTe/GCE, but lower at 7.4 ± 0.5 μF for the GCE, which is consistent with a higher electrochemically active surface area for the NiTe-modified GCE. Likewise, the CPE element, with an exponent of 0.5 for the NiTe/GCE, is consistent with a diffusion-controlled reaction. On the other hand, the CPE has a higher exponent of 0.7 for the GCE, indicating a more complex process. The R_{ct} was computed as 5.55 kΩ for NiTe/GCE and 10.0 kΩ for the unmodified GCE. Similarly, the R_2 element was obtained as 86.9 and 208 kΩ for NiTe/GCE and CGE, respectively. These data clearly show that the NiTe/GCE is more conductive.

To assess the increase in electroactive surface area (ECSA), hexaammineruthenium(III) chloride $[Ru(NH_3)_6]^{3+}$ in 0.1 M NaCl was used as a redox probe. The ferri/ferrocyanide system was initially used, but was later avoided due to potential electrostatic repulsion caused by oxide formation on the surface of NiTe, which imparts a negative charge and hinders electron transfer with the negatively charged ferri/ferrocyanide system. The ECSA of the prepared electrode was determined using the Randles−Sevcik relationship, eq 2.

$$I_p = (2.69 \times 10^5) n^{3/2} A D^{1/2} \upsilon^{1/2} C \quad (2)$$

Here, n is the number of electrons involved in the redox reaction, I_p is the peak current, A is the ECSA (cm^2), υ is the scan rate ($V\ s^{-1}$), D is the diffusion constant of the $[Ru(NH_3)_6]^{3+}$ probe ($9.1 \times 10^{-6}\ cm^2\ s^{-1}$),[26,27] and C is the bulk concentration of the analyte. The slope of the plot of I_p vs $\upsilon^{1/2}$ was used to determine the ECSA of the NiTe/GCE. A potential window between 0.2 V and −0.7 V (vs SCE) was employed, and various scan rates were used to record the CVs, as shown in Figure 4c for the NiTe/GCE. These CVs are consistent with enhanced electron transfer efficiency, as

https://doi.org/10.1021/acsanm.5c03794
ACS Appl. Nano Mater. 2025, 8, 20523−20533

Scheme 1. Reduction Mechanism of RON at NiTe/GCE

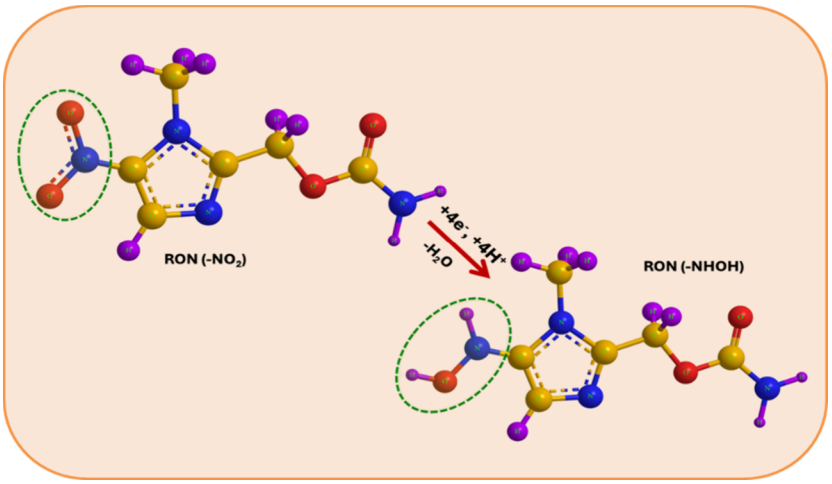

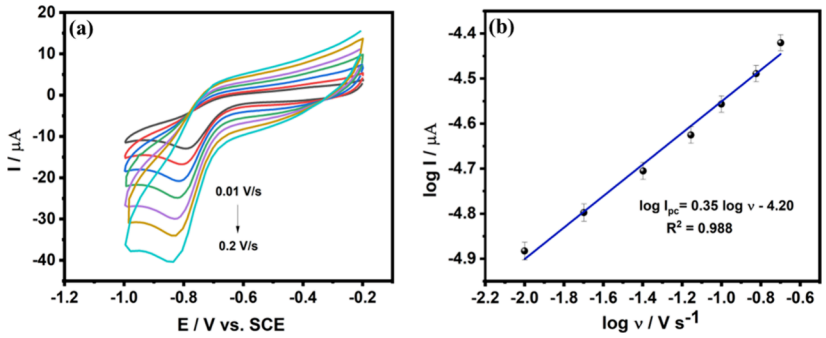

Figure 6. (a) CVs of NiTe/GCE at different scan rates from 10 to 200 mV s^{-1} recorded in 300 μM RON at pH 8.0, (b) linear plot of the logarithm of the peak current against the logarithm of the scan rate.

evidenced by the peak-to-peak separation of 79 mV, which is closer to the ideal value of 59 mV, in comparison to the 102 mV separation observed for the unmodified GCE. The corresponding plot for the GCE is shown in Figure S2.

The scan rate was varied from 10 to 170 mV s^{-1} to calculate the ECSA of bare GCE and NiTe/GCE. Linear plots were obtained for both systems as shown in Figure 4d, with the peak currents plotted against the square root of the scan rate, which is characteristic of a diffusion-controlled process. The linear regression equation and correlation coefficient were observed as I_p (μA) = 2.42 × 10^{-4} $\upsilon^{1/2}$ ($V^{1/2}$ $s^{-1/2}$) + 1.703, R^2 = 0.999 for NiTe/GCE and I_p (μA) = 1.61 × 10^{-4} $\upsilon^{1/2}$ ($V^{1/2}$ $s^{-1/2}$) + 4.09, R^2 = 0.999 for GCE. After substituting values into eq 2, the value of A was calculated for bare GCE as 0.043 cm^2, and for NiTe/GCE as 0.096 cm^2. This shows that the surface area increases by approximately a factor of 2.23, on modifying the GCE with NiTe NPs.

The CV technique was used to evaluate the electrocatalytic performance of the NiTe-modified GCE in the presence of RON, at a pH of 8.0 and at a scan rate of 75 mV s^{-1}. As shown in Figure 5a, no reduction peaks appeared in the CV recorded for NiTe/GCE in KOH without RON, confirming that the observed irreversible electrochemical response is due to RON, as illustrated in Scheme 1. Although the reduction of nitro groups is generally represented as a $4e^-/4H^+$ process leading to the formation of hydroxylamine (−NHOH), in alkaline media such as 0.05 M KOH, the required protons are not derived from free H^+ ions but rather from water molecules, which serve as the proton donors. This proton-coupled electron transfer mechanism has been widely reported for nitroaromatic and nitroimidazole compounds.[28] The assignment of a $4e^-$ pathway is consistent with established literature on RON reduction, where sequential electron and proton transfers yield the hydroxylamine intermediate.

To further investigate the electrochemical behavior of RON, DPV was conducted under the same conditions. Figure 5b presents the DPV results, comparing the response of the bare GCE and NiTe/GCE. The NiTe/GCE exhibits a much higher peak current than the bare GCE, indicating increased electrocatalytic activity toward the reduction of RON. Also, for the bare GCE, the reduction peak potential for RON was observed at −0.75 V. In comparison, the peak potential for the NiTe/GCE in RON was lower at −0.71 V, indicating a more thermodynamically viable process at the modified electrode. Also, a strong current response was observed for RON detection using NiTe/GCE at a pH of 8.0. Under these experimental conditions, good reproducibility was achieved, as indicated by the RSD% values in Table S1 (supporting data), which were well below 5%.

To establish the optimal pH, the pH was varied from 6.0 to 11.0, and the corresponding DPVs are shown in Figure 5c. The highest reduction peak current was observed at a pH 8.0, indicating more favorable electrochemical activity under these conditions. At lower pH (pH 6 and 7), the reduction peaks occur at more negative potentials, with a lower current. Likewise, at higher pH values of 9 to 11, the peak current decreases. These changes may be related to the stability of the NiTe NPs. At higher pH values, soluble tellurium-based oxides

https://doi.org/10.1021/acsanm.5c03794
ACS Appl. Nano Mater. 2025, 8, 20523−20533

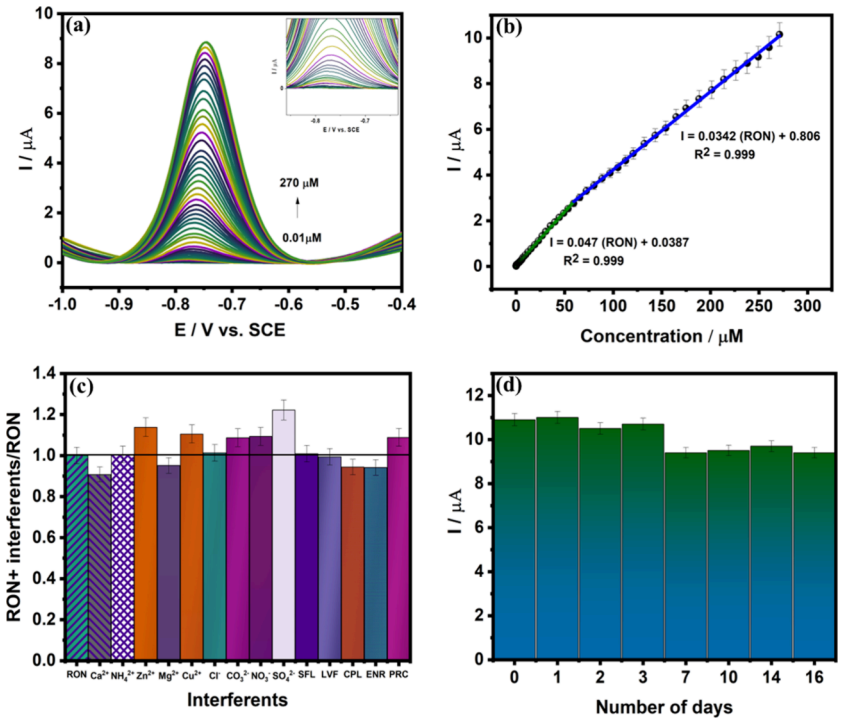

Figure 7. (a) DPVs recorded at pH 8.0 with various concentrations of RON from 10 nM to 270 μM, (b) calibration curve plotted of the DPV peak currents against the RON concentration, (c) selectivity with the ratio of the peak current with and without the interferent with a 100 μM RON solution and 1 mM interferent ions and 200 μM drugs, (d) peak current as a function of days stored in 300 μM RON.

Table 1. Comparison of the NiTe/GCE Sensor with Previously Reported Sensors for the Electrochemical Detection of RON[a]

electrode material	technique	linear range/μM	LOD/nM	sensitivity/μA μM^{-1} cm^{-2}
$CoCo_2O_4$ NR/h-BN/GCE[29]	DPV	0.01−1345	3	5.845
Zn-CrLDH/Ni−Co-sulfide)[13]	DPV/EIS	0.01−297; 297−2187	1.12.6	0.374
CPT-BDD[30]	SWAdCSV	12.70−63.40;76.04−126.2	2550	0.15
Ni-doped $CoMoO_4$ microrods[31]	CV	0.05−200	15	1.57
PraseodymiumTungstate[14]	CV	0.001−20.4	0.3	7.72
NiTe/GCE (This work)	DPV	0.01−60; 60−270	1.5	0.489

[a]NR-nanorods; h-BN-hexagonal-boron nitride; LDH-layered double hydroxides; CPT-BDD- cathodic pretreatment- boron-doped diamond.

and $Ni(OH)_2$ species may form, leading to partial dissolution and lower peak currents, as well as less favorable peak potentials. This variation between pH and peak current is further highlighted in Figure 5d, clearly showing that the optimal pH is 8.0. Therefore, pH 8.0 was selected for all sensing studies, as it not only provides the highest peak current but is also closely related to the natural pH conditions of environmental water samples.

The electrochemical behavior of the NiTe/GCE sensor with the RON was examined by analyzing its response at different scan rates. As shown in Figure 6a, the scan rates were systematically increased from 10 to 200 mV s^{-1} in an electrolytic solution containing 300 μM of RON. A linear graph of peak current versus the square root of scan rate was plotted and is shown in the Figure S3, yielding the regression equation I (μA) = 70.16 $\upsilon^{1/2}$ (V s^{-1})$^{1/2}$ + 5.76 with a correlation coefficient R^2 = 0.996, which provides evidence for a characteristic diffusion-controlled process for the electrochemical sensing of RON with the NiTe/GCE. The linear plot of the logarithm of the peak current as a function of the logarithm of the scan rate is shown in Figure 6b with a slope of 0.35. The linear equation obtained was log I (I/μA) = 0.35 log υ (υ/V s^{-1}) − 4.20, R^2 = 0.988, indicating diffusion control, with a gradient close to 0.5, as opposed to a value of 1.0 that would suggest adsorption control.

The analytical response of the NiTe/GCE sensor was investigated through calibration, selectivity, and recovery studies. DPV measurements were carried out over a broad concentration range of 0.01 to 270 μM, as illustrated in Figure 7a. The experiment was performed in the presence of N_2-saturated solution at a pH of 8.0. As the analyte concentration increased, a corresponding rise in peak current was observed, indicating a strong electrochemical response. The resulting linear calibration curve, shown in Figure 7b, demonstrates an extended linear range from 0.01 to 270 μM. Using the well-known expression for the limit of detection (LOD), where the LOD = 3σ/slope from the calibration curve, the LOD was calculated as 1.5 nM using the lower concentration linear range. The linear regression analysis gave the equations: I_p (μA) = 0.047 [RON] (μM) + 0.0387, R^2 = 0.999 for the lower region and I_p (μA) = 0.034 [RON] (μM) + 0.806, R^2 = 0.999, indicating a direct proportionality between current and analyte concentration across the tested range. The sensitivity was computed as 0.489 μA μM^{-1} cm^{-2} for the lower concentration range using the estimated electroactive surface area of 0.096 cm^2. The analytical performance of the NiTe/GCE is

https://doi.org/10.1021/acsanm.5c03794
ACS Appl. Nano Mater. 2025, 8, 20523−20533

compared in Table 1 with sensors that have been reported previously. These sensors include zinc−chromium layered double hydroxide with nickel cobalt sulfide (ZC/NCS) composites and $CoCo_2O_4$ nanorod/hexagonal boron nitride (*h*-BN) modified glassy carbon electrodes for sensing RON. These sensors show LODs as low as 1.1−3.0 nM, and sensitivities up to 5.845 $\mu A\ \mu M^{-1}\ cm^{-2}$. Compared to these, the NiTe/GCE sensor in this work shows an LOD of 1.5 nM, demonstrating comparable and excellent nanomolar detection performance for the NiTe NPs, while also maintaining a wide linear range up to 300 μM and a sensitivity of 0.489 $\mu A\ \mu M^{-1}\ cm^{-2}$.

The selectivity of the NiTe/GCE sensor was evaluated in the presence of common ions typically found in natural water samples. In Figure 7c, 1 mM of each potential interferent was added to a 100 μM RON solution, resulting in a 10:1 interferent-to-analyte concentration ratio. The peak current ratio between the response to 100 μM RON alone and that in the presence of each interferent was determined. Figure 7d shows the peak currents of the NiTe/GCE sensor during consecutive measurements in 300 μM RON at pH 8.0 over 16 days. The consistent peak currents, with an average of 10.13 μA and a maximum of 10.9 μA, reflect strong repeatability. A low relative standard deviation of 0.70% highlights the reliability of the sensor and its potential for stable, repeated use. This good stability is further evident in Figure S4, where the DPVs recorded before and after the 16 days are compared. The current is somewhat lower. However, there is little evidence of any significant changes in the profile of the DPV peak.

To evaluate the selectivity of NiTe/GCE for detecting RON, the potential interfering substances commonly present in natural aquatic environments were investigated. These include widely used antibiotics, such as sulfanilamide (SFL), levofloxacin (LVF), ciprofloxacin (CPL), and paracetamol (PRC), at 200 μM concentration compared to 100 μM of RON. A series of inorganic ions, i.e., Cu^{2+}, Ca^{2+}, Zn^{2+}, Mg^{2+}, NH_4^+, NO_3^-, CO_3^{2-}, Cl^-, and SO_4^{2-} at 1.0 mM concentrations, which are 10-fold in excess of RON, were also included in the test. Electrochemical responses were recorded with and without the presence of these interferents, and the relative change in peak current was used as a measure of selectivity. The results are shown in Figure 7c, and demonstrate that the current responses show minimal variations on the addition of most of the competing ions or drugs. The most significant interference is evident in the presence of the sulfates. It is unlikely that sulfate ions are directly reduced under the present conditions (at a pH of 8.0, potential of −0.71 V vs SCE). Instead, the stronger response is more likely due to sulfate ions interacting with the NiTe electrode surface and altering the double layer or interfacial charge transfer, which can facilitate electron transfer to RON. For the other systems, the minimal deviation in peak current values between the pure RON solution and those containing interferents demonstrates that the NiTe/GCE sensor retains excellent selectivity, even in the presence of common inorganic ions and pharmaceutical compounds.

In addition, the performance of the NiTe/GCE was further validated through selectivity evaluation and recovery tests conducted using spiked tap and river water samples. All water samples were first centrifuged and filtered through a 0.45 μm membrane or filter paper to remove particulate matter. KOH was then added to the sample to adjust the pH to 8.0, matching the optimal sensing conditions. The sample was then spiked using 50, 100, 200, and 300 μM concentrations of the target analyte, approximately covering the linear range of the sensor. The spiked samples were then analyzed using DPV. Each concentration recovery test was conducted in triplicate to ensure reproducibility. The recovery values are summarized in Table 2, and range from 90.7 to 108.3% for tap water and from 90.8 to 106.2% for river water. Low relative standard deviations (RSD < 5%) were achieved, denoting that the sensor performs reliably in complex water matrices.

Table 2. Recovery Studies Were Performed with Tap and River Water Samples

sample	added Drug (μM)	found Drug (μM)	recovery (%)	RSD (%)
Tap water	50	45.4	90.8	0.08
	100	97.0	97.0	2.39
	200	216.6	108.3	4.80
	300	321.9	107.3	3.61
Real river water	50	51.8	103.6	1.29
	100	103.3	103.3	4.26
	200	212.4	106.2	1.24
	300	272.4	90.8	6.3

CONCLUSIONS

In this work, we developed NiTe NPs supported on a GCE as a highly sensitive and selective platform for the electrochemical detection of RON, a nitroimidazole antibiotic of growing environmental concern. The NiTe NPs, synthesized through a simple hydrothermal route, exhibited well-defined crystalline morphology and a high electroactive surface area, which enhanced electron transfer and facilitated efficient RON reduction. As a result, the sensor achieved an ultralow detection limit of 1.5 nM, a wide linear range of 0.01−270 μM, and good sensitivity, along with excellent selectivity, reproducibility, and stability. Application to spiked tap and river water samples further demonstrated reliable recovery, confirming the robustness of the sensor in complex matrices. Importantly, this study establishes, for the first time, the use of NiTe NPs for antibiotic detection, expanding the scope of telluride-based materials beyond previously reported applications such as biomolecule sensing. By addressing key challenges in morphology, composition, and electrode-nanoparticle interface optimization, this work not only highlights NiTe as an underutilized yet highly promising material but also contributes a new strategy for monitoring emerging antibiotic contaminants. The findings highlight the potential of telluride-based nanomaterials to advance the field of electrochemical sensing and support the development of practical, low-cost platforms for environmental monitoring and public health protection.

ASSOCIATED CONTENT

Supporting Information

The Supporting Information is available free of charge at https://pubs.acs.org/doi/10.1021/acsanm.5c03794.

TEM image of NiTe NPs and particle size distribution histogram, peak current vs square root of scan rate in 300 μM RON, CVs of GCE in $Ru(NH_3)_6^{3+}$, DPVs of NiTe/GCE after 0 and 16 days of immersion in 300 μM RON and reproducibility (PDF)

https://doi.org/10.1021/acsanm.5c03794
ACS Appl. Nano Mater. 2025, 8, 20523−20533

AUTHOR INFORMATION

Corresponding Author

Carmel B. Breslin − *Department of Chemistry and Kathleen Lonsdale Institute, Maynooth University, Maynooth, Co. Kildare W23F2H6, Ireland;* orcid.org/0000-0002-0586-5375; Email: Carmel.Breslin@mu.ie

Authors

Tara Barwa − *Department of Chemistry, Maynooth University, Maynooth, Co. Kildare W23F2H6, Ireland*

Ramaraj Sukanya − *Department of Chemistry, Maynooth University, Maynooth, Co. Kildare W23F2H6, Ireland;* orcid.org/0000-0002-9033-4201

Thamaraiselvi Kanagaraj − *School of Chemical Engineering, Yeungnam University, Gyeongsan, Gyeongbuk 38541, Republic of Korea*

Gillian Collins − *Department of Chemistry, Maynooth University, Maynooth, Co. Kildare W23F2H6, Ireland*

Yiran Luo − *Department of Chemistry, Maynooth University, Maynooth, Co. Kildare W23F2H6, Ireland;* orcid.org/0000-0003-0937-8387

Eithne Dempsey − *Department of Chemistry and Kathleen Lonsdale Institute, Maynooth University, Maynooth, Co. Kildare W23F2H6, Ireland*

Raj Karthik − *Department of Chemistry, Maynooth University, Maynooth, Co. Kildare W23F2H6, Ireland;* orcid.org/0000-0002-8605-643X

Jae-Jin Shim − *School of Chemical Engineering, Yeungnam University, Gyeongsan, Gyeongbuk 38541, Republic of Korea;* orcid.org/0000-0002-8027-9886

Complete contact information is available at: https://pubs.acs.org/10.1021/acsanm.5c03794

Notes

The authors declare no competing financial interest.

ACKNOWLEDGMENTS

This publication has emanated from research conducted with the financial support of Research Ireland under grant numbers SFI/20/FFP-P/8793 and IRC/GOIPG/2022/1605, the Sustainable Energy Authority of Ireland, grant number SEAI/22/RDD/841, and the EU Horizon 2020 program under the Marie Skłodowska-Curie grant No. 101106064. The authors would also like to thank Esther Adegoke, Bernal Institute, University of Limerick, Ireland, for recording the TEM data.

REFERENCES

(1) Lee Ventola, C. The Antibiotic Resistance Crisis: Part 1: Causes and Threats. *P&T* **2015**, *40* (4), 277−283.

(2) Getahun, H. Antimicrobial Resistance. In *Global Health Essentials*; Raviglione, M. C. B.; Tediosi, F.; Villa, S.; Casamitjana, N.; Plasència, A., Eds.; Sustainable Development Goals Series; Springer International Publishing: Cham, 2023; pp 143−147.

(3) Tornimbene, B.; Eremin, S.; Escher, M.; Griskeviciene, J.; Manglani, S.; Pessoa-Silva, C. L. WHO Global Antimicrobial Resistance Surveillance System Early Implementation 2016−17. *Lancet Infect. Dis.* **2018**, *18* (3), 241−242.

(4) Kümmerer, K. Antibiotics in the Aquatic Environment - A Review - Part I. *Chemosphere* **2009**, *75* (4), 417.

(5) Liang, M.; Liu, Y.; Lu, S.; Wang, Y.; Gao, C.; Fan, K.; Liu, H. Two-Dimensional Conductive MOFs toward Electrochemical Sensors for Environmental Pollutants. *TrAC, Trends Anal. Chem.* **2024**, *177*, No. 117800.

(6) Lu, S.; Wang, Q.; Fang, L.; Zheng, X.; Yin, F.; Liu, H. Bimetallic Platinum-Nickel Nanoparticles Modified on the Screen-Printed Electrode for Highly Sensitive Urea Determination. *IEEE Sensors J.* **2024**, *24* (4), 4221−4227.

(7) Meng, X.; Dong, X.; Liu, D.; Niu, Q.; Lu, S.; You, T. Rapid Electrochemical Sensing of Zn(II) Using MesoporousMnO_2 @N-Graphene Composites. *IEEE Sensors J.* **2023**, *23* (21), 25673−25679.

(8) Wang, Q.; Xue, Q.; Chen, T.; Li, J.; Liu, Y.; Shan, X.; Liu, F.; Jia, J. Recent Advances in Electrochemical Sensors for Antibiotics and Their Applications. *Chin. Chem. Lett.* **2021**, *32* (2), 609−619.

(9) Laghlimi, C.; Moutcine, A.; Chtaini, A.; Isaad, J.; Soufi, A.; Ziat, Y.; Amhamdi, H.; Belkhanchi, H. Recent Advances in Electrochemical Sensors and Biosensors for Monitoring Drugs and Metabolites in Pharmaceutical and Biological Samples. *ADMET DMPK* **2018**, *11* (2), 151.

(10) Hong, J.; Su, M.; Zhao, K.; Zhou, Y.; Wang, J.; Zhou, S.-F.; Lin, X. A Minireview for Recent Development of Nanomaterial-Based Detection of Antibiotics. *Biosensors* **2023**, *13* (3), No. 327.

(11) Mahugo-Santana, C.; Sosa-Ferrera, Z.; Torres-Padrón, M. E.; Santana-Rodríguez, J. J. Analytical Methodologies for the Determination of Nitroimidazole Residues in Biological and Environmental Liquid Samples: A Review. *Anal. Chim. Acta* **2010**, *665* (2), 113−122.

(12) Han, C.; Chen, J.; Wu, X.; Huang, Y.; Zhao, Y. Detection of Metronidazole and Ronidazole from Environmental Samples by Surface Enhanced Raman Spectroscopy. *Talanta* **2014**, *128*, 293−298.

(13) Priya, T. S.; Chen, T.-W.; Chen, S.-M.; Kokulnathan, T.; Lou, B.-S.; Ullah, R.; Al-onazi, W. A.; Elshikh, M. S. 3D Architectured Zinc-Chromium Layered Double Hydroxide with Nickel Cobalt Sulfide Composite for the Electrochemical Detection of Ronidazole. *Environ. Sci.: Nano* **2024**, *11* (5), 2021−2035.

(14) Velmurugan, M.; Sakthi Priya, T.; Chen, T.-W.; Chen, S.-M.; Kokulnathan, T.; Chuang, H.-Y.; Ahmed, F.; Hussain, A.; Husain Khan, Z. Sustainable Synthesis of Praseodymium Tungstate: An Electrochemical Probe for Detection of Ronidazole. *Microchem. J.* **2024**, *201*, No. 110657.

(15) Pimpilova, M. A Brief Review on Methods and Materials for Electrode Modification: Electroanalytical Applications towards Biologically Relevant Compounds. *Discovery Electrochem.* **2024**, *1* (1), 12.

(16) Guo, M.; Gu, S.; Xu, S.; Lu, J.; Wang, Y.; Zhou, G. Design, Synthesis and Application of Two-Dimensional Metal Tellurides as High-Performance Electrode Materials. *Front. Chem.* **2022**, *10*, No. 1023003.

(17) Tremel, W.; Kleinke, H.; Derstroff, V.; Reisner, C. Transition Metal Chalcogenides: New Views on an Old Topic. *J. Alloys Compd.* **1995**, *219* (1−2), 73−82.

(18) Majhi, K. C.; Yadav, M. Transition Metal-Based Chalcogenides as Electrocatalysts for Overall Water Splitting. *ACS Eng. Au* **2023**, *3* (5), 278−284.

(19) Kshetri, T.; Singh, T. I.; Lee, Y. S.; Khumujam, D. D.; Kim, N. H.; Lee, J. H. Metal Organic Framework-Derived Cobalt Telluride-Carbon Porous Structured Composites for High-Performance Supercapacitor. *Compos. B Eng.* **2021**, *211*, No. 108624.

(20) Wang, Z.-Y.; Shen, C.-H.; Yang, S.-H.; Chang, H.-W.; Tsai, Y.-C. $CoNiTe_2$ Nanomaterials as an Efficient Non-Enzymatic Electrochemical Sensing Platform for Detecting Dopamine. *Chemosensors* **2024**, *12* (6), No. 110.

(21) Mayilmurugan, M.; Rajamanickam, G.; Perumalsamy, R.; Sivasubramanian, D. Nickel Cobalt Telluride Nanorods for Sensing the Hydrogen Peroxide in Living Cells. *ACS Omega* **2022**, *7* (17), 14556−14561.

(22) Golrokh Amin, B.; De Silva, U.; Masud, J.; Nath, M. Ultrasensitive and Highly Selective Ni_3Te_2 as a Nonenzymatic Glucose Sensor at Extremely Low Working Potential. *ACS Omega* **2019**, *4* (6), 11152−11162.

(23) Fatima, B.; Saeed, U.; Hussain, D.; Jawad, S.-Z.; Rafiq, H. S.; Majeed, S.; Manzoor, S.; Qadir, S. Y.; Ashiq, M. N.; Najam-ul-Haq, M. Facile Hydrothermal Synthesis of NiTe Nanorods for Non-Enzymatic Electrochemical Sensing of Whole Blood Hemoglobin in Pregnant Anemic Women. *Anal. Chim. Acta* **2022**, *1189*, No. 339204.

(24) Farid, A.; Pan, L.; Usman, M.; Khan, I. A.; Khan, A. S.; Ahmad, A. U.; Javid, M. In-Situ Growth of Porous CoTe2 Nanosheets Array on 3D Nickel Foam for Highly Sensitive Binder-Free Non-Enzymatic Glucose Sensor. *J. Alloys Compd.* **2021**, *861*, No. 158642.
(25) Kulandaivel, L.; Park, J.; Sivakumar, P.; Jung, H. Hydrazine-Assisted Hydrothermal Synthesis of NiTe and $NiTe_2$ Nanorods. *J. Mater. Sci: Mater. Electron.* **2023**, *34* (20), 1557.
(26) Trachioti, M. G.; Lazanas, A. Ch.; Prodromidis, M. I. Shedding Light on the Calculation of Electrode Electroactive Area and Heterogeneous Electron Transfer Rate Constants at Graphite Screen-Printed Electrodes. *Microchim Acta* **2023**, *190* (7), 251.
(27) Kinkelin, S.-J.; Röder, F.; Vogel, K.; Steimecke, M.; Bron, M. A Fundamental Study on Cyclic Voltammetry at Porous Carbon Thin-Film Electrodes. *Electrochim. Acta* **2024**, *488*, No. 144183.
(28) Fotouhi, L.; Faramarzi, S. Voltammetric Studies on Nitro Radical Anion Formation from Furazolidone and Kinetic of the Coupled Chemical Reaction. *J. Electroanal. Chem.* **2004**, *568*, 93−99.
(29) Karupppaiah, B.; Jeyaraman, A.; Chen, S.-M.; Huang, Y.-C. Development of Highly Sensitive Electrochemical Sensor for Antibiotic Drug Ronidazole Based on Spinel Cobalt Oxide Nanorods Embedded with Hexagonal Boron Nitride. *Electrochim. Acta* **2023**, *446*, No. 142008.
(30) Bettio, G.; Okumura, L.; Silva, R.; Silva, T. Development of an Electroanalytical Method for Ronidazole Determination in Environmental and Food Matrices Using Boron-Doped Diamond Electrode. *J. Braz. Chem. Soc.* **2024**, No. e20230162.
(31) Karuppaiah, B.; Jeyaraman, A.; Chen, S.-M.; Chavan, P. R.; Karthik, R.; Shim, J.-J.; Park, S. J. Design and Synthesis of Nickel-Doped Cobalt Molybdate Microrods: An Effective Electrocatalyst for the Determination of Antibiotic Drug Ronidazole. *Environ. Res.* **2023**, *222*, No. 115343.

https://doi.org/10.1021/acsanm.5c03794
ACS Appl. Nano Mater. 2025, 8, 20523−20533